PHYSICAL REVIEW B **103**, 054106 (2021)

Breaking of inversion symmetry in $NdGaO_3$

Binoy Krishna De,[1] Vivek Dwij,[1] Mayanak K. Gupta,[2] Ranjan Mittal,[2,3] Himal Bhatt,[4] V. R. Reddy,[1] and V. G. Sathe[1,*]
[1] *UGC-DAE Consortium for Scientific Research, University Campus, Khandwa Road, Indore 452001, India*
[2] *Solid State Physics Division, Bhabha Atomic Research Centre, Mumbai 400085, India*
[3] *Homi Bhabha National Institute, Anushaktinagar, Mumbai 400094, India*
[4] *High Pressure & Synchrotron Radiation Physics Division, Bhabha Atomic Research Centre, Mumbai 400085, India*

(Received 3 August 2020; accepted 22 January 2021; published 8 February 2021)

$NdGaO_3$ (NGO) is an important substrate material often used in depositing functional oxide thin films. We have carried out temperature-dependent polarized Raman and infrared spectroscopy studies along with theoretical calculations on single-crystal NGO, which revealed a structural phase transition from centrosymmetric space group *Pbnm* to noncentrosymmetric space group $Pbn2_1$ at ~200 K. The microscopic origin of the phase transition is extracted using a unique protocol involving polarized Raman spectroscopy (PRS) studies carried out as a function of crystallographic orientation. Here, we demonstrate the power of PRS in probing directional atomic rearrangements across the phase transition.

DOI: 10.1103/PhysRevB.103.054106

I. INTRODUCTION

In modern technological applications, thin films are the backbone of many devices. Thin films show several exotic physical properties depending on the crystal structure and strain present in the films which are basically determined by the underlying substrate used for the thin-film deposition. The substrate's crystal structure plays a very crucial role in defining the physical properties of the thin films. Therefore, the crystal structure of the substrate and its thermal stability over the entire operating temperature range of the thin-film base devices are extremely important for their applications. As a substrate material, $NdGaO_3$ (NGO) is greatly used for depositing thin films of several kinds of materials such as high-temperature superconductors [1], multiferroic compounds [2], and to make GaN-based optical devices [3] and spintronic devices [4], etc. In addition to thin-film applications, the thermal stability of NGO is also important for using it as an interconnecting material in solid oxide fuel cells which are operating in the temperature range from 77 to 1000 K [5]. The crystal structure is also important for understanding the physical properties shown by doped NGO systems such as ionic conductivity and UV-blue light emission [6,7]. On the other hand, optical applications require the knowledge of the molecular structure and vibrational properties of the substrate, since the penetration depth of the radiation is often greater than the film thickness.

NGO crystallizes in a perovskite structure with tilted and distorted oxygen octahedra leading to an orthorhombic structure with ferroelastic properties [8,9]. However, the exact crystal symmetry and thermal evolution of the crystal structure is still debatable. Several authors refined the x-ray diffraction (XRD) and neutron diffraction data collected on powder and single-crystal NGO by considering the centrosymmetric *Pbnm* space group [10–12]. On the other hand, some considered the competing space group $Pbn2_1$, which also fitted well with the experimental data [13–15]. The difference between these two space groups is minor, in that one mirror plane is absent in the $Pbn2_1$. Due to the absence of one of the mirror planes, the centrosymmetry is broken in $Pbn2_1$. In such a situation, it is very difficult to conclusively determine the crystal structure by using normal diffraction methods [16]. Previously, optical studies such as Raman, infrared (IR), and ellipsometry were performed on single-crystal NGO at room temperature along with the density functional theory (DFT) calculations. While these results were found to be consistent with the centrosymmetric *Pbnm* space group [17–19], Saine *et al.* used the $Pbn2_1$ space group in their (DFT) calculations of the normal mode of vibrations at room temperature [20]. Temperature (T)-dependent XRD and neutron diffraction studies showed that the $Pbnm/Pbn2_1$ are stable structures in the temperature range from room temperature to 12 K without any structural transition [10,14]. However, the T evolution of the b-lattice parameter obtained from the refinement of the XRD data showed an anomalous change ~200 K (hereafter it is referred to as T_c). The T-dependent spectroscopic measurements could not detect any abrupt change around T_c [14,21,22], although some new weak modes were reported below T_c. Savytskii *et al.* [19] reported weak anomalous changes around T_c in the dielectric loss and magnetic susceptibility measurements. The appearance of new weak modes and a subtle anomaly in the T-dependent b-lattice parameter, dielectric loss, and magnetic susceptibility of single-crystal NGO [10,23] hints at a structural modification around T_c [24–26]. As the substrate of NGO is greatly used for depositing multiferroic and superconducting thin films, knowledge of the presence or absence of centrosymmetry is crucial. To clarify this issue and the temperature evolution of the crystal structure, we have

---

[*] Corresponding author: vasant@csr.res.in

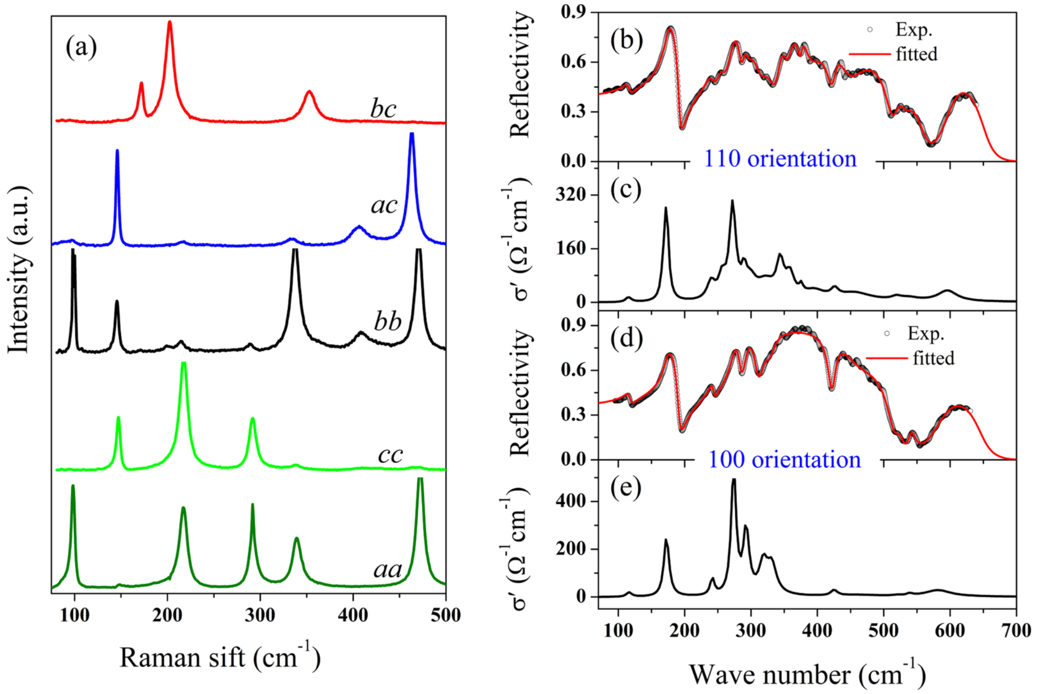

FIG. 1. The Raman and IR spectra at 300 K. (a) Raman spectra were collected on a (100)-oriented single crystal in several polarization configurations. (b) and (d) IR spectra collected on (110)- and (100)-oriented single crystals in the reflection mode. The red line represents the curve fitted using the Lorentz oscillator model and the resultant optical conductivities σ' are shown in (c) and (e), respectively.

performed T-dependent polarized Raman spectroscopy and IR spectroscopy studies along with DFT calculations using both centrosymmetric *Pbnm* and noncentrosymmetric $Pbn2_1$ space groups. According to the spectroscopic selection rules [27], in centrosymmetric crystals the Raman and IR modes are mutually exclusive while they may simultaneously appear in a spectrum when the inversion symmetry breaks. According to the Friedel criteria, it is well known that normal diffraction measurements are unable to distinguish between the *Pbnm* and $Pbn2_1$ space groups, and in such a situation complementary Raman and IR spectroscopy can be very efficient tools to detect the presence of an inversion center in a system [28,29]. In this paper, we show that the NGO belongs to the centrosymetric *Pbnm* space group at room temperature and the transformation to the noncentrosymmetric $Pbn2_1$ space group below T_c is caused by distortion in the oxygen octahedra. The microscopic atomic rearrangements responsible for this phase transition across T_c were probed using a polarized Raman spectroscopy (PRS) study.

II. EXPERIMENT

Commercially procured $NdGaO_3$ single-crystal substrates (MTI Corporation, USA) of (100) and (110) orientation were used in the present study. The orientation of the crystallographic unit cell axes was determined from XRD θ-2θ and φ-scan measurements on (111), (112), (204), and (220) reflections with χ values of 50.48°, 59.82°, 54.61°, and 44.63°, respectively, using a PAN analytical X'PERT high-resolution x-ray diffraction (HRXRD) system equipped with a Cu anode. Polarized Raman measurements were performed using a micro-Raman spectrometer (Horiba Jobin-Yvon) equipped with a 473-nm excitation laser, 1800-g/mm grating, an edge filter for Rayleigh line rejection, and a CCD detector

TABLE I. Parameters of A_g Raman modes in a centrosymmetric *Pbnm* structure obtained from DFT calculations (ω_{calc}) and experimental spectra (ω_{expt}) at 300 K collected in the *aa*, *bb*, and *cc* polarization configurations in comparison with previous reports. I_{RS} represents experimental Raman intensity while S_{RS} represents theoretically obtained Raman scattering activity.

Parameter	$l = 1$	2	3	4	5	6	7
ω_{expt}[a]	96.27(2)	145.20(1)	215.04(4)	290.02(4)	337.53(7)	408.2(3)	470.32(2)
ω_{expt}[b]	96	145	215	290	337	414	470
ω_{calc}[a]	95.7	133.6	201.6	278.4	330.6	389.8	430.5
ω_{calc}[b]	94.3	153.4	232.4	293.5	345.4	421.2	468.9
(B_{2g})[a]	6.39(5)	2.58(3)	13.00(5)	5.69(5)	6.99(9)	4.98(9)	13.80(8)
S_{RS} (B_{2g})[b]	2.040	1.707	14.54	21.34	16.12	7.766	32.94

[a] This work.

[b] Taken from Ref. [17].

TABLE II. Parameters of B_{1g} Raman modes in a centrosymmetric *Pbnm* structure obtained from DFT calculations (ω_{calc}) and experimental spectra (ω_{expt}) at 300 K collected in the *ab* polarization configurations in comparison with previous reports. I_{RS} represents experimental Raman intensity while S_{RS} represents theoretically obtained Raman scattering activity.

Parameter	$l = 1$	2	3	4	5	6	7
ω_{expt}[a]		152.9(1)	215.4(0)	363.7(1)	448.4(2)		
ω_{expt}[b]	110	151	213	362	448		
ω_{calc}[a]	105.2	142.4	212.3	333.5	407.5	458.2	623.5
ω_{calc}[b]	113.0	159.3	230.7	370.2	443.6	518.6	676.6
$I_{\text{RS}}(B_{2g})$[a]		0.21(2)	14.9(1)	0.78(6)	0.43(4)		
$S_{\text{RS}}(B_{2g})$[b]	0.063	0.555	41.64	3.561	6.768	0.232	0.001

[a] This work.

[b] Taken from Ref. [17].

giving a spectral resolution of $\sim$1 cm^{-1}. The laser was focused to a spot size of $\sim$1 μm diameter onto the flat surface of the sample using a 50× objective lens. The spectra were collected in backscattering geometry. PRS spectra were collected by mounting the sample on a rotatable sample stage with a 0°–360° angle marker in parallel and cross-polarization geometry. The incident laser light was plane polarized while the detection was done either in a parallel or cross-polarization mode using an analyzer. A set of Raman spectra was collected either in a parallel or cross-polarization configuration when the incident direction of polarization with respect to the crystal axis was kept at a desired angle by rotating the sample stage. We have used the Porto notations for defining the polarization configurations [30]. Low-temperature Raman spectroscopy measurements were carried out using a temperature control (THMS600, Linkam, U.K.) with 0.1° temperature stability. The low-temperature infrared spectroscopic measurements were performed using a continuous-flow liquid-helium cryostat (Oxford Optistat CF-V). The cryostat consisted of polythelene windows and was mounted on a near normal incidence (11°) reflection accessory. The whole setup was mounted on the sample stage of a Bruker Vertex 80V Fourier-transform infrared (FT-IR) spectrometer equipped with a far infrared - deuterated trigycine sulphate detector. These constitute parts of the infrared beamline (BL-6) facility at Indus-1, India. The specimen crystals were mounted on the cold finger of the cryostat and the temperature was varied from 350 to 4 K in small steps. The temperature was controlled using a proportional–integral–derivative controller and gas flow was monitored using a gas flow meter calibrated for helium gas. The sample chamber was evacuated to a vacuum of the order of 0.0001 mbar before cooling. For background correction, all the experiments were carried out using a gold mirror at the same temperature points. All the measurements were carried out in the same pressure environment using an unpolarized beam. The spectra were recorded at a resolution of 4 cm^{-1} and a total of 200 scans were coadded in all the samples as well as background measurements to cover the far-IR spectral range from 30 to 650 cm^{-1}. The obtained IR reflectance spectra were used to determine the optical conductivity spectra at various temperatures by using the Kramer-Kronig transformation employing Drude-Lorentz formulations [31].

III. THEORETICAL CALCULATION METHODS

For phonon calculations we have chosen a 2 × 2 × 2 supercell in both the *Pbnm* and $Pbn2_1$ space groups. We have performed the phonon calculation using the supercell method as implemented in PHONOPY software [32]. It is used for generating supercell and subsequent atomic displacements. The structure optimizations for NGO in the *Pbnm* and $Pbn2_1$ space groups were carried out by using density functional the-

TABLE III. Parameters of B_{2g} Raman modes in a centrosymmetric *Pbnm* structure obtained from DFT calculations (ω_{calc}) and experimental spectra (ω_{expt}) at 300 K collected in the *ac* polarization configurations in comparison with previous reports. I_{RS} represents experimental Raman intensity while S_{RS} represents theoretically obtained Raman scattering activity.

Parameter	$l = 1$	2	3	4	5
ω_{expt}[a]	144.03(1)	331.3(3)	404.9(1)	461.23(1)	
ω_{expt}[b]	144	334	405	463	
ω_{calc}[a]	122.2	288.3	397.1	423.5	652.2
ω_{calc}[b]	151.9	330.8	417.4	456.7	701.1
$I_{\text{RS}}(B_{2g})$[a]	4.13(2)	0.96(6)	4.99(8)	13.70(4)	
$S_{\text{RS}}(B_{2g})$[b]	1.775	0.001	17.95	22.17	0.089

[a] This work.

[b] Taken from Ref. [17].

TABLE IV. Parameters of B_{3g} Raman modes in a centrosymmetric *Pbnm* structure obtained from DFT calculations (ω_{calc}) and experimental spectra ω_{expr}) at 300 K collected in the *bc* polarization configurations in comparison with previous reports. I_{RS} represents experimental Raman intensity while S_{RS} represents theoretically obtained Raman scattering activity.

Parameter	$l = 1$	2	3	4	5
ω_{expt}[a]	169.5(3)	200.42(1)	350.83(6)		
ω_{expt}[b]	170	200	351		
ω_{calc}[a]	154.2	197.3	323.1	386.8	595.6
ω_{calc}[b]	170.3	197.8	361.8	417.7	625.5
$I_{\text{RS}}(B_{2g})$[a]	3.04(3)	17.27(5)	7.48(6)		
$S_{\text{RS}}(B_{2g})$[b]	0.007	20.32	11.99	3.098	1.302

[a] This work.

[b] Taken from Ref. [17].

TABLE V. TO phonon mode parameters with A_u symmetry (silent mode) in a centrosymmetric *Pbnm* structure obtained from DFT calculations (ω_{calc}) in comparison with previous reports.

Parameter	$l = 1$	2	3	4	5	6	7	8
ω_{calc} [a]	80.1	150.3	181.8	230.4	272.6	336.0	522.9	543.2
ω_{calc} [b]	94.76	170.45	193.88	270.14	296.32	366.78	558.06	585.84

[a] This work.

[b] Taken from Ref. [17].

ory calculations implemented under the generalized gradient approximation (GGA) as implemented in the Vienna *ab initio* simulation package (VASP) [33,34]. The generalized gradient approximation with the Perdew, Burke, and Ernzerhof [35,36] (PBE) functional implemented in VASP has been used for the exchange correlation energy. The convergence criteria for total energy and forces were set to 10^{-8} eV and 10^{-4} eV/Å respectively. A $4 \times 4 \times 4$ K-point mesh was generated according to the Monkhorst-Pack (MP) scheme [37]. The energy cutoff was set to 900 eV. To account for the magnetic degree of freedom of the Nd atom, we have chosen a pseudopotential with the f electron in the valence shell. The valence electronic configurations of O, Ga, and Nd are $2s^2 2p^4$, $4s^2 4p^1$, and $5S^2 6S^2 5p^6 5d^1 4f^3$, respectively. The compound is known to undergo a transition to the antiferromagnetic state which takes place at about 1 K [38]. The structure relaxation is performed by including A-type antiferromagnetic configurations for the Nd ions. The calculated total energy of both the phases (centrosymmetric *Pbnm* and noncentrosymmetric $Pbn2_1$) at $T = 0$ is found to be nearly the same (−154.045 eV/20 atoms). However, a different contribution of vibrational and magnon entropies will stabilize the noncentrosymmetric $Pbn2_1$ phase at low temperature.

IV. RESULT AND DISCUSSIONS

NGO single crystals were characterized by using XRD, Raman, and IR spectroscopic measurements. A specific number of well-defined sharp peaks in the XRD and φ scan on several reflections (Fig. S1 [39]) established that the NGO single crystals are of good quality without any twin domains.

Figure 1(a) shows the Raman spectra collected on the (100)-oriented single crystal in various polarization configurations. The polarization behavior is consistent with the selection rules. Figures 1(b) and 1(d) show the IR spectra collected on the (110)- and (100)-oriented single crystals, respectively, at 300 K. The red curve represents the fitting done using the Lorentz oscillator model [31]. The optical conductivity as a function of wave number derived from the IR spectra is presented in Figs. 1(c) and 1(e), respectively. The room-temperature Raman and IR spectra match well with previous reports [18]. According to the factor group analysis, the irreducible representation of lattice vibrations for the *Pbnm* structure is given as [18]

$$\Gamma_{\mathrm{total}} = [7A_g + 7B_{1g} + 5B_{2g} + 5B_{3g}](\mathrm{r}) + 8A_u(\mathrm{n}) \\ + [7B_{1u} + 9B_{2u} + 9B_{3u}](\mathrm{ir}) + [B_{1u} + B_{2u} + B_{3u}](\mathrm{ac}),$$

while for the $Pbn2_1$ structure the irreducible representation is given as [22]

$$\Gamma_{\mathrm{total}} = 15A_2(\mathrm{r}) + [14A_1 + 14B_1 + 14B_2](\mathrm{r, ir}) \\ + [A_1 + B_1 + B_2](\mathrm{ac}),$$

where r represents Raman-active modes, ir the infrared-active modes, ac the acoustic modes, and n the silent modes.

TABLE VI. TO phonon mode parameters with B_{1u} symmetry polarized along the c axis in a centrosymmetric *Pbnm* structure obtained from DFT calculations (ω_{calc}) and experimental IR spectra (ω_{expr}) at 300 K in comparison with previous reports. ω_p and γ represent the oscillator strength and linewidth of the IR modes. ε_∞ values obtained from fitting are 3.8(1) and 4.0(4) for (100)- and (110)-oriented samples, respectively.

Parameter	$l = 1$	2	3	4	5	6	7
ω_{expt} [a]	168(1)	172.7(3)	272.2(5)	292.6(5)	318.4(4)	538.9(9)	595.8(7)
ω_p [a]	192(6)	336(3)	440(7)	415(10)	337(12)	79(4)	260(3)
γ [a]	8(2)	7.2(5)	11(1)	10.7(9)	14(1)	12(1)	35(1)
ω_{expt} (TO) [b]	166.0(3)	170.8(1)	269.8(1)	290.9(7)	342.0(2)	550.(3)	591.(3)
ω_{expt} [c]	167.6		272.1	289.0	346.3		596.3
ω_p [c]	472.1		472.9	368.2	664.5		295.7
γ [c]	11.7		4.1	12.2	15.7		23.6
ω_{calc} (TO) [a]	134.5	150.8	244	274.4	322.1	521.3	557.5
ω_{calc} (LO) [a]	150.7	173.5	265.8	282.1	473.1	524.4	616.1
ω_{calc} (TO) [b]	165.99	185.36	272.36	294.00	354.41	563.01	585.27
ω_{calc} (LO) [b]	166.36	198.72	288.90	320.91	516.83	565.22	648.36

[a] This work.

[b] Taken from Ref. [17].

[c] Taken from Ref. [41].

TABLE VII. TO phonon mode parameters with B_{2u} symmetry polarized along the b axis in a centrosymmetric *Pbnm* structure obtained from DFT calculations (ω_{calc}) and experimental IR spectra (ω_{expt}) at 300 K in comparison with previous reports. ω_p and γ represent the oscillator strength and linewidth of the IR modes.

Parameter	$l = 1$	2	3	4	5	6	7	8	9
ω_{expt} [a]	116(1)	172(3)	241.6(9)	273.8(5)	292.6(5)	318.4(6)	426.0(8)	519(1)	581(1)
ω_p [a]	104(10)	376(4)	179(13)	530(9)	415(10)	337(12)	139(5)	98(5)	277(3)
γ [a]	9(2)	9.3(5)	7(1)	8.8(8)	10.7(9)	14(1)	13(1)	14(2)	47
ω_{expt} (TO) [b]	116.0(6)	172.7(4)	240.3(7)	277.3(8)	293.7(0)	314.(6)	428.(4)	538.(9)	573.(3)
ω_{expt} [c]	116.0	173.0	240.0	276.6	293.5	314.3	427.4	538.7	574.6
ω_p [c]	104.7	368.8	251.4	551.7	518.7	418.0	178.3	166.1	279.4
γ [c]	2.9	4.1	6.1	6.4	8.6	17.9	8.1	7.9	35.3
ω_{calc} (TO) [a]	109.7	160.6	222.7	264.2	273.8	287.8	394.9	450.5	531.6
ω_{calc} (LO) [a]	111.5	174.0	231.2	267.4	287.4	383.7	424.7	485	586.6
ω_{calc} (TO) [b]	124.41	182.59	244.80	282.00	297.33	318.17	431.31	527.12	572.34
ω_{calc} (LO) [b]	125.49	192.28	249.48	289.05	314.56	423.03	492.25	542.28	645.12

[a] This work.
[b] Taken from Ref. [17].
[c] Taken from Ref. [41].

Raman spectra were fitted using Lorentz functions and the obtained parameters of various modes are listed in Tables I–IV in comparison with a previous report by Mock *et al.* In order to obtain the IR phonon mode parameters, IR reflectivity spectra were fitted using the classical Lorentz oscillator model described by Zang *et al.* [40]. In this model, the dielectric function $\tilde{\varepsilon}(\omega)$ $[(= n + ik)^2]$ of a material in the infrared region can be described as [41]

$$\tilde{\varepsilon}(\omega) = \tilde{\varepsilon}(\infty) + \sum_{j=1}^{N} \frac{\omega_p^2}{\omega_j^2 - \omega^2 - i\omega\Gamma_j}, \tag{1}$$

where $\tilde{\varepsilon}(\infty)$ is the high-frequency dielectric constant, N is the number of phonon modes, and ω_p, ω_j, and Γ_j are the strength, central frequency, and linewidth of the j th transverse optical (TO) phonon, respectively. The spectra were fitted with Eqs. (1) together with Fresnel's formula which can be written in quasinormal incident of light as $R(\omega) = |\frac{\sqrt{\tilde{\varepsilon}(\omega)}-1}{\sqrt{\tilde{\varepsilon}(\omega)}+1}|^2$ [40]. The solid red lines in Figs. 1(b) and 1(d) represent the fitted curves for the reflectivity data (black circle) at 300 K using this model. The complex dielectric function $\tilde{\varepsilon}(\omega) = \varepsilon' + i\varepsilon''$ was calculated by fitting the reflectivity (shown in Fig. S3). The obtained optical conductivity $\sigma'(= \varepsilon_0\omega\varepsilon'')$ [shown in Figs. 1(c) and 1(e)] provides the phonon mode positions which are listed in Tables VI–VIII. For the sake of comparison, phonon mode frequencies reported previously are also given. The assignment of the observed phonon modes is performed based on the reports by Mock *et al.* [17] and Hofer *et al.* [41].

It is seen in Figs. 1(a)–1(e) that the Raman and IR modes are mutually exclusive at 300 K, which confirms the centrosymmetric structure at 300 K. The lattice dynamical calculations of phonon modes with a *Pbnm* structure (shown in Tables I–VIII) show a good match with our experimental values, which further confirms the centrosymmetric *Pbnm* structure at 300 K [17]. We have also compared our experimental and calculated phonon frequencies with previous calculations by Mock *et al.* [17], which show a fair agreement,

TABLE VIII. TO phonon mode parameters with B_{3u} symmetry polarized along the a axis in a centrosymmetric *Pbnm* structure obtained from DFT calculations (ω_{calc}) and experimental IR spectra (ω_{expt}) at 300 K in comparison with previous reports. ω_p and γ represent the oscillator strength and linewidth of the IR modes.

Parameter	$l = 1$	2	3	4	5	6	7	8	9
ω_{expt} [a]		172.7(3)	256(1)	273.8(5)	299(1)	344(1)	375(1)	426(1)	595.8(7)
ω_p [a]		336(3)	213(19)	530(8)	245(13)	282(11)	100(9)	139(5)	260(3)
γ [a]		7.2(5)	12(3)	8.8(8)	20(2)	13(1)	7(1)	13(1)	35(1)
ω_{expt} (TO) [b]	114.(6)	175.0(9)	253.3(0)	274.8(5)	304.9(0)	351.5(7)	369.3(7)	530.(1)	606.4(8)
ω_{expt} [c]		175.5	252.8	276.5	304.0	348.9	367.6		607.8
ω_p [c]		371.7	300	593.2	376.6	189.4	640.5		234.6
γ [c]		3.9	5.5	8.1	14.5	7.6	15.4		30.3
ω_{calc} (TO) [a]	108.1	161.4	237.6	253.8	291.9	319.8	350.5	414.7	558.3
ω_{calc} (LO) [a]	108.7	175.5	246.2	283.7	294.7	322.9	414.7	508.9	599
ω_{calc} (TO) [b]	121.44	181.61	259.14	279.60	303.76	348.77	384.33	455.01	606.99
ω_{calc} (LO) [b]	121.55	193.94	263.94	300.07	334.90	349.52	454.70	560.73	656.49

[a] This work.
[b] Taken from Ref. [17].
[c] Taken from Ref. [41].

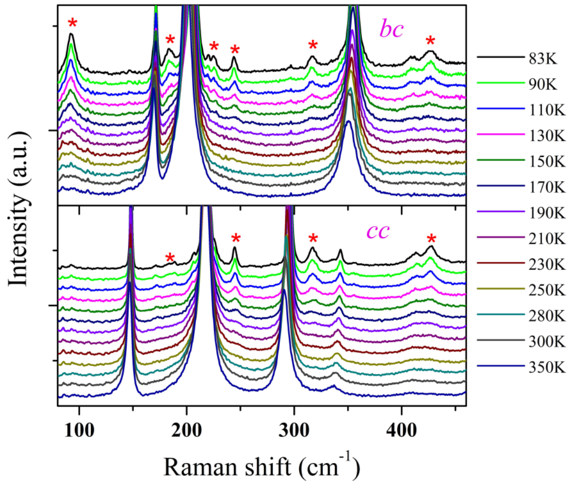

FIG. 2. Temperature-dependent Raman spectra in *bc* and *cc* polarization configurations. Stars indicate extra modes appearing below T_c.

although our calculated values are slightly underestimated from Mock *et al.*'s calculations. This could be due to the different level of approximation used in these two DFT calculations. Mock *et al.* have performed phonon calculations with a local density approximation (LDA) parametrized by Perdew and Zunger, whereas in this work the calculations were performed within the GGA approximation formulated with the PBE scheme. The different level of approximation and parametrization of the exchange correlation functional leads to the difference in volume and bond lengths and is reflected in the calculated phonon frequencies. It may be noted that the lattice parameters and volume are slightly different between the two calculations. The Mock *et al.* calculations give an underestimated volume (223.70 Å^3) with respect to experimental values (230.95 Å^3), while our calculation gives slightly overestimated values (239.23 Å^3). Further, due to the presence of the strongly correlated f-electron element Nd, we included the magnetic degree of freedom to achieve the closest experimental volume. This may further lead to differences between the two calculation results. Our calculations along with those performed by Mock *et al.* [17] are in agreement with the experimental data.

To obtain the T evolution of the crystal structure, Raman spectra from 350 down to 83 K were collected in several polarization configurations. Figure 2 shows the T dependency of the Raman modes collected in $a(bc)\bar{a}$ and $a(cc)\bar{a}$ polarization configurations. Here, the symbol in parentheses denotes the direction of the polarization of the incident and detected beam while the outside symbols denote the direction of the incident and detected photon. In short, these will be denoted as *bc* and *cc* polarization configurations, respectively. The orientation of the crystallographic unit cell axes with respect to the electric field polarization direction is very crucial in polarized Raman spectroscopic measurements. For the same it was necessary to obtain *in situ* information of the orientation of the crystal through azimuthal angle-dependent polarized Raman spectroscopy. The intensity of the Raman modes in different polarization configurations and thus as a function of the azimuthal angle can be calculated by invoking Raman tensors.

Raman tensors for different normal modes corresponding to the D_{2h} point group are defined as [42]

$$A_g = \begin{pmatrix} a & 0 & 0 \\ 0 & b & 0 \\ 0 & 0 & c \end{pmatrix}, \quad B_{1g} = \begin{pmatrix} 0 & d & 0 \\ d & 0 & 0 \\ 0 & 0 & 0 \end{pmatrix},$$

$$B_{2g} = \begin{pmatrix} 0 & 0 & e \\ 0 & 0 & 0 \\ e & 0 & 0 \end{pmatrix}, \quad B_{3g} = \begin{pmatrix} 0 & 0 & 0 \\ 0 & 0 & f \\ 0 & f & 0 \end{pmatrix}, \tag{2}$$

where a-f are tensor elements. For backscattering geometry used in the present study, the laser is incident along the Z axis and the scattered light is detected along the $-Z$ axis of the laboratory frame of reference (XYZ) as shown in Fig. 3. The unit vector of the electric field of incident light along the Y axis (say) can be given as

$$e_i^{\|} = (0\ \ 1\ \ 0), \quad e_s^{\|} = \begin{pmatrix} 0 \\ 1 \\ 0 \end{pmatrix}, \quad e_s^{\perp} = \begin{pmatrix} 1 \\ 0 \\ 0 \end{pmatrix}. \tag{3}$$

The Raman intensity can be calculated using the following expression:

$$I \propto (e_i R e_s)^2. \tag{4}$$

The variation of Raman intensity as a function of azimuthal angle ψ (in-plane rotation angle) was calculated by using the Euler transformation and Eq. (4) and can be given as

$$\begin{aligned} &I_{A_g}^{\|} \propto (b\cos^2\psi + c\sin^2\psi)^2, && I_{A_g}^{\perp} \propto \left(\frac{(b-c)\sin 2\psi}{2}\right)^2, \\ &I_{B_{1g}}^{\|} = 0, && I_{B_{1g}}^{\perp} = 0, \\ &I_{B_{2g}}^{\|} = 0, && I_{B_{2g}}^{\perp} = 0, \\ &I_{B_{3g}}^{\|} \propto (f\sin 2\psi)^2, && I_{B_{3g}}^{\perp} \propto (f\cos 2\psi)^2. \end{aligned} \tag{5}$$

Raman spectra with parallel and cross-polarization configurations are collected on a (100) surface at room temperature as a function of azimuthal (in-plane) angle ψ and fitted with Lorentz functions. Figure 3(a) shows Raman spectra collected in a parallel polarization configuration as a function of ψ. Figure 3(b) shows the measurement geometry. The experimental intensity obtained by fitting is shown in Figs. 3(c)–3(e) for specific A_g and B_{3g} modes. The solid (red) lines represent the behavior of the intensity as a function of ψ obtained using Eq. (5). The intensities of the A_g and B_{3g} modes show twofold and fourfold degeneracy, respectively, as a function of ψ. This provided the exact direction of the crystallographic axes. The main aim of this study is to locate the crystallographic b axis and then carry out a temperature-dependent study with incident light polarization parallel to this axis. Equation (5) shows that in the bb ($\psi = 0^\circ$) and cc ($\psi = 90^\circ$) polarization configurations, the A_g mode intensity depends only on the tensor elements b and c, respectively. The azimuthal angle

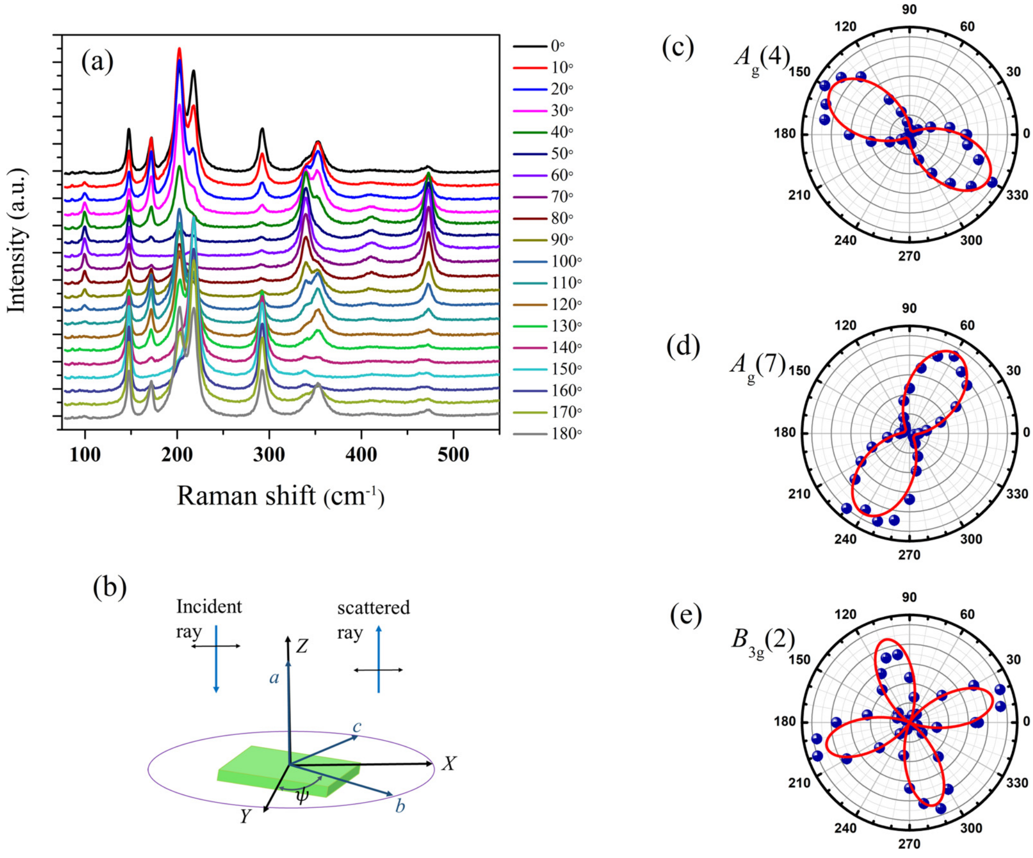

FIG. 3. (a) The Raman spectra collected at various azimuthal angles in the parallel polarization configuration. (b) Schematic representation of the measurement geometry. *abc* and *XYZ* represent the crystallographic and laboratory frame of references, respectively. (c)–(e) represent the intensity variations of the specific A_g and B_{3g} modes, respectively, as a function of azimuthal angle ψ in the parallel polarization configuration.

dependency of the Raman intensity of different modes (Fig. 3) confirms the good alignment of the crystal in the temperature-dependent Raman studies [43].

As the temperature was reduced, a number of new peaks (marked by a red star in Fig. 2) appear below T_c, which strengthen with a further lowering of the temperature. The symmetries of the new modes have been determined by the polarization analysis and are listed in Tables IX–XII. The new mode at $89\,cm^{-1}$ was previously attributed to the electronic excitations between the crystal-field levels of the Nd^{3+} ion [10]. The unusual T dependence of this mode was explained [10] by considering coupling between the electronic excitation (at 89 cm^{-1}) of A_g symmetry and the phonon mode located at $96\,cm^{-1}$ [$A_g(1)$] with the same symmetry. However, the appearance of a number of other new peaks as seen in Fig. 2 hints towards a lowering of symmetry below T_c. As mentioned before, some authors expressed the possibility of the noncentrosymmetric space group $Pbn2_1$, though they could not confirm it through structural investigations [13]. In order to confirm the existence of noncentrosymmetry, T-dependent IR spectroscopy studies have been performed on (100)- and (110)-oriented single crystals.

Figure 4 shows the T evolution of the IR spectra. In this study also a few extra modes (marked by red arrows) appear at $T < T_c$. In order to facilitate the comparison of Raman and IR modes below T_c, the Raman spectra in various polarization configurations at 90 K and IR spectra collected at 90 K on (110) and (100) orientation and the corresponding optical conductivity are plotted in Fig. 5. Interestingly, numerous modes are clearly seen to be simultaneously present in both Raman and IR spectra at 90 K (marked by a red star), which is allowed according to selection rules only when the crystal shows a noncentrosymmetric space group. The polarization dependence and temperature evolution of the spectral profile of the new modes (except for the $89\,cm^{-1}$ mode) are also found to be consistent with the normal behavior of phonons (for example, see Fig. 6).

The frequency and the symmetry of the phonon modes deduced from the theoretical first-principles calculations using the $Pbn2_1$ space group also match well with the experimental results (Tables IX–XII). Therefore, the simultaneous presence of phonon modes in both Raman and IR spectra below T_c provides direct experimental evidence of a structural phase transition from a room-temperature centrosymmetric ($Pbnm$) phase to the noncentrosymmetric ($Pbn2_1$) phase below T_c.

To the best of our knowledge, in NGO, no soft mode is reported so far. Our theoretical lattice dynamical calculations also have not given any imaginary phonon frequency related to the soft mode in the $Pbnm$ structure. This indicates that the orthorhombic $Pbnm$ phase is not only energetically stable but also a dynamically stable structure and therefore should be the ground state of the NGO. However, our present results clearly show a centrosymmetric to noncentrosymmetric phase transition. Thus, in order to find out the detailed microscopic lattice

TABLE IX. TO phonon mode parameters with A_2 symmetry in the noncentrosymmetric $Pbn2_1$ structure obtained from DFT calculations (ω_{calc}) and experimental Raman spectra (ω_{expt}) at 90 K in comparison with previous reports. Raman spectra (RS) collected in the *ab* polarization configuration. # represents the new modes in the Raman spectra that were observed by Kamishima *et al.* [22].

Parameter	$l = 1$	2	3	4	5	6	7	8	9	10	11	12	13	14	15
ω_{expt} [a]	89.32(5)			155.4(0)		219.12(0)				364.81(1)		453.71(4)			
ω_{calc} [b]	89#			155	183#	219				365		453			
ω_{calc} [a]	80.3	105.0	142.0	150.3	181.2	212.2	230.3	272.5	330.6	334.9	407.3	458.3	520.1	543.5	623.4
ω_{calc} [c]	68	75	88	148	158	190	298	306	343	366	417	446	514	552	617

[a] This work.
[b] Taken from Ref. [22] at 21 K.
[c] Taken from Ref. [20].

dynamics across the phase transition, we have performed temperature-dependent polarized Raman spectroscopy (PRS) studies across T_c under a unique protocol.

As mentioned in the experimental section, under the PRS protocol the Raman spectra were collected in various incident angles of the polarization with respect to the crystallographic axes and the scattered beam was analyzed either in parallel polarization (*aa*, *bb*, *cc*) or cross-polarization (*ab*, *bc*, *ac*) configurations. The recorded Raman spectra using this protocol were fitted using the Lorentz profile function after correcting the spectra for the Bose-Einstein thermal factor [44] (the fitting is shown in Fig. S2 [39]). Figure 7(a) shows the geometry of *T*-dependent PRS measurements in the *bb* and *cc* polarization configurations. Figures 7(b)–7(d) show the *T* evolution of the full width at half maximum (FWHM) of the $A_g(6)(408\,\mathrm{cm}^{-1})$, $A_g(4)(290\,\mathrm{cm}^{-1})$, and $A_g(7)(470\,\mathrm{cm}^{-1})$ modes collected in the *bb* polarization configuration. The red line represents the fitted anharmonic curve for four phonon decay process [45]. The temperature variation of the FWHM of the $A_g(4)$ and $A_g(6)$ modes deviates from anharmonic behavior below T_c, i.e., the phonon lifetime changes below T_c, which signifies the structural modification at T_c. On the other hand, the octahedral stretching mode $A_g(7)$ does not show any change in the whole temperature range. In this *bb* polarization configuration, the *T* dependence of intensity of the $A_g(4)$ and $A_g(6)$ modes [Fig. 7(f)] also changes at T_c, whereas the intensity of the $A_g(7)$ mode [Fig. 7(g)] varies almost linearly with *T* in the whole studied temperature range. On the other hand, in the *cc* polarization configuration, the intensities of all the A_g modes show a monotonous *T* dependence in the complete temperature range [Fig. 7(e)].

According to Eq. (5), the Raman tensor elements *b* and *c* are the only contributory terms in the intensities of the A_g mode ($I^{\parallel}_{A_g}$) for the *bb* ($\psi = 0^\circ$) and *cc* ($\psi = 90^\circ$) configurations, respectively. As such, the Raman tensor element is expected to show a monotonic decrease with decreasing *T*. Thus, the distinct change in the intensity and FWHM only in the *bb* polarization configuration across T_c indicates that the Raman tensor element *b* changes significantly across T_c. On the other hand, a linear variation of the Raman intensity in the *cc* polarization configuration as seen in Fig. 7(e) depicts a monotonous *T* dependence of the Raman tensor element *c* in the studied temperature range. It is well known that the Raman tensor element represents the polarizability derivative in a specific direction and for nondegenerate phonon modes of highly insulating samples such as NGO, it is likely to show a variation with a variation in interatomic distances [27,46,47]. Therefore, the Raman intensity measured in a particular polarization configuration may be affected by the changes associated with the variation in the interatomic distances or the lattice strain component [48]. Thus, in an orthogonal (orthorhombic) system, the anomalous variation in the Raman tensor element *b* across T_c is directly related to the variation in the interatomic distance along the crystallographic *b* axis (detailed discussions are found in the Supplemental Material [39]). Similarly, the monotonous *T* dependence of the Raman tensor element *c* indicates a monotonous *T* dependence of the *c*-lattice parameter. Previous temperature-dependent XRD

TABLE X. TO phonon mode parameters with A_1 symmetry in the noncentrosymmetric $Pbn2_1$ structure obtained from DFT calculations (ω_{calc}) and experimental Raman and IR spectra (ω_{expt}) at 90 K in comparison with previous reports. Transition moments associated with the IR modes are parallel to the *c* axis and the Raman spectra collected in the *aa*, *bb*, and *cc* polarization configurations. The asterisk indicates the mode which was observed in both the Raman (RS) and IR spectra.

Parameter	$l = 1$	2*	3*	4*	5	6*	7	8*	9*	10*	11	12	13	14
ω_{expt} (RS) [a]	103.1(0)	148.1(1)	171.2(2)	184.1(4)	218.8(0)	244.6(2)	272.6(2)	295.7(0)	318.1(2)	343.1(0)	413.2(2)	471.2(0)		
ω_{expt} (IR) [a]		147 (6)	174 (1)	183 (1)		243.6(4)	274.1(4)	293.6(2)	319.4(7)	344.9(5)			542 (1)	595 (1)
ω_{expt} (RS) [b]	104	148			217			297			414	474		
ω_{calc} (TO) [a]	77.9	102.9	132.3	158.9	202.3	238.2	261.7	275.2	315.2	351.2	391.1	442.0	521.4	557.8
ω_{calc} (LO) [a]	89.9	130.4	136.3	184.5	202.4	261.6	273.6	295.3	331.2	384.0	417.1	467.7	527.2	619.1
ω_{calc} (TO) [c]	68	87	113	148	158	194	301	328	367	391	430	458	543	620

[a] This work.
[b] Taken from Ref. [22] at 21 K.
[c] Taken from Ref. [20].

TABLE XI. TO phonon mode parameters with B_1 symmetry in the noncentrosymmetric $Pbn2_1$ structure obtained from DFT calculations (ω_{calc}) and experimental Raman and IR spectra (ω_{expt}) at 90 K in comparison with previous reports. Transition moments associated with the IR modes are parallel to the *a* axis and the Raman spectra collected in the *ac* polarization configuration. The asterisk indicates the mode which was observed in both the Raman (RS) and IR spectra in our study. # represents the new modes in the Raman spectra that were observed by Kamishima *et al.* [22].

Parameter	$l = 1^*$	2*	3*	4	5*	6	7	8	9*	10	11	12*	13	14
ω_{expt} (RS)[a]	93.5(1)	146.6(0)	171.2(2)		244.6(1)			335.2(6)	345.0(1)		413.6(0)	429.4(4)	466.8(0)	
ω_{expt} (IR)[a]	92(2)	147(6)	174(1)		259(3)	274.1(4)	302.9(5)		343.9(5)	375(1)		427.2(5)		595(1)
ω_{expt} (RS)[b]	91#	146						336			412	425#	466	
ω_{calc} (TO)[a]	109.4	153.8	160.1	196.8	222.2	263.9	274.4	287.3	323.0	385.4	394.1	451.1	531.6	595.7
ω_{calc} (LO)[a]	112.2	153.8	173.3	196.8	232.4	267.7	286.5	323.0	385.3	389.6	420.3	481.2	588.2	595.8
ω_{calc}[c]	75	90	130	216	298	311	333	339	371	398	438	509	542	553

[a] This work.
[b] Taken from Ref. [22] at 21 K.
[c] Taken from Ref. [20].

studies on this system showed the monotonic behavior of *a*- and *c*-lattice parameters with *T* and an anomalous variation of the *b*-lattice parameter below T_c [10]. Therefore, our PRS study (Fig. 7) is able to precisely decipher the anomalous changes in the *b*-lattice parameter. According to Cui *et al.* [49], polarized Raman spectroscopy is highly sensitive in detecting a structural phase transition; and prominent changes in the Raman mode intensity and FWHM across a T_c can be considered as a signature of a structural phase transition. Thus, the change in intensity and FWHM of Raman modes in the *bb* configuration signifies a structural phase transition at T_c . Further, the intensity of the $A_g(4)$ and $A_g(6)$ Raman modes in the *bb* configuration above T_c are fitted with a linear function [Fig. 7(f)] and extrapolated down to 80 K. The slope of this fitted linear equation is, say, α_1. The deviation of the experimental intensity from the extrapolated intensity was deduced by subtraction and plotted as a function of *T* in Fig. 8. The deviation of the intensity below T_c is also fitted with a linear equation and the slope of this line is, say, $\alpha_{\mathrm{deviation}}$. Therefore, the relative (normalized) change in the slope of the Raman intensity can be given as

$$\alpha_{\mathrm{norm}} = \frac{\alpha_{\mathrm{deviation}}}{\alpha_1}. \tag{6}$$

The obtained values of $\alpha_1, \alpha_{\mathrm{deviation}}$, and α_{norm} for the $A_g(4)$ and $A_g(6)$ phonon modes are listed in Table XIII. The relative change in the slope of the intensity of the Raman modes in the *bb* configuration was found to scale with the relative change in the slope of the *b*-lattice parameter deduced from XRD measurements [10] (see Table XIII). This one-to-one correspondence between the Raman intensity and the lattice parameter gives a pathway to find atomic rearrangements across the structural phase transitions using PRS under this unique protocol.

It may be noted that the variation in the lattice parameter is extremely small and is in the order of 0.001 Å, but still Raman measurements could easily detect the associated changes in lattice vibrations. Therefore, very minute changes in the lattice parameters or interatomic distances in a particular direction of the orthogonal system can be precisely monitored by using the PRS method under the defined protocol, however, a precise estimation of changes in the lattice parameters or strains from the change in the phonon mode frequency [50–53] across the phase transition requires knowledge of the symmetry, stress/strain relations, and the mode Grüneisen parameter or deformation potentials related to the two phases. Since Raman spectroscopy is a local probe [54–56], this method can be used to monitor the variation

TABLE XII. TO phonon mode parameters with B_2 symmetry in the noncentrosymmetric $Pbn2_1$ structure obtained from DFT calculations (ω_{calc}) and experimental Raman and IR spectra (ω_{expt}) at 90 K in comparison with previous reports. Transition moments associated with the IR modes are parallel to the *b* axis and the Raman spectra collected in the *bc* polarization configuration. The asterisk indicates the mode which was observed in both the Raman (RS) and IR spectra. # represents the new modes in the Raman spectra that were observed by Kamishima *et al.* [22].

Parameter	$l = 1^*$	2	3*	4	5*	6*	7*	8	9	10*	11	12*	13	14
ω_{expt} (RS)[a]	94.0(2)		171.3(0)		184.8(4)	205.9(1)	244.0(3)			318.1(2)	355.3(0)	426.6(2)		
ω_{expt} (IR)[a]	92(2)	119.7(8)	169(1)	174(1)	184.1(4)	195(1)	243.6(4)	274.1(4)	293.6(2)	319.6(6)		427.2(5)	519(1)	581(1)
ω_{expt} (RS)[b]	90#		171		183#	206					355			
ω_{calc} (TO)[a]	108.1	122.1	160.9	237.9	253.1	287.6	291.8	319.4	349.3	397.0	414.6	422.6	557.9	651.2
ω_{calc} (LO)[a]	109.2	122.1	177.5	243.6	281.2	288.0	292.7	232.6	397.0	414.0	422.5	513.1	596.1	651.2
ω_{calc}[c]	68	86	130	188	215	226	324	338	357	398	434	455	533	545

[a] This work.
[b] Taken from Ref. [22] at 21 K.
[c] Taken from Ref. [20].

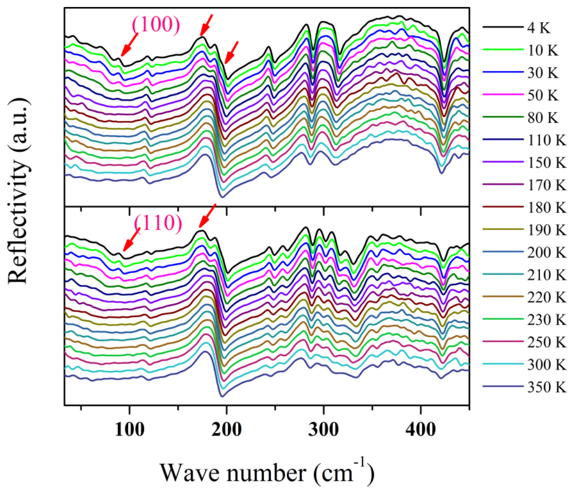

FIG. 4. Temperature-dependent IR spectra collected on NGO (100) and (110) single crystals. The red arrow indicates the new IR modes observed below T_c. The spectra have been offset for clarity.

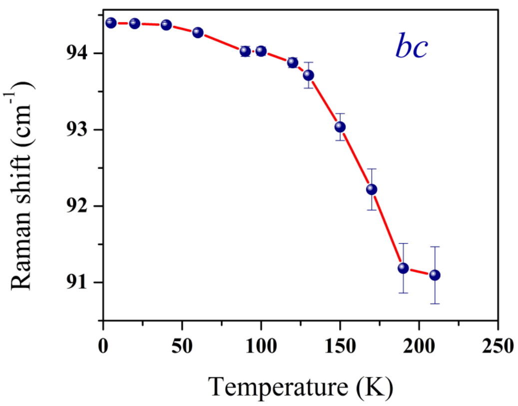

FIG. 6. T-dependent Raman shift of new mode $B_2(1)$.

in interatomic distances present in the system even at short length scales.

In order to understand the microscopic reason or the driving force for the structural phase transition across T_c as detected by PRS studies, the lattice dynamical picture of the Raman modes showing changes around T_c were estimated by theoretical calculations and presented in Fig. 9. It is seen that the $A_g(4)$ mode represents a relative vibration of Nd and O atoms along the b axis and the $A_g(6)$ mode represents out-of-phase octahedral bending vibrations [57], whereas the $A_g(7)$ mode represents in-phase octahedral stretching in the ab plane [57]. It is worth noting here that, while the $A_g(4)$ and $A_g(6)$ modes involve vibrations of the apical oxygen atoms, the apical oxygen in the $A_g(7)$ mode remains stationary and only the oxygen atoms lying in the basal plane (ab plane) of the octahedra take part in the vibrations. It is also to be noted that the $A_g(4)$ mode (Fig. 1) is observed in the aa, bb, and cc polarization configurations. As mentioned earlier, the intensity of a Raman mode in a specific polarization configuration is influenced by the change in polarizability along a specific direction. Thus, the intensity of this mode in the aa, bb, and cc polarization configurations can be considered as a reflection of change in atomic displacement along the a, b, and c axes, respectively. On the other hand, the $A_g(7)$ mode

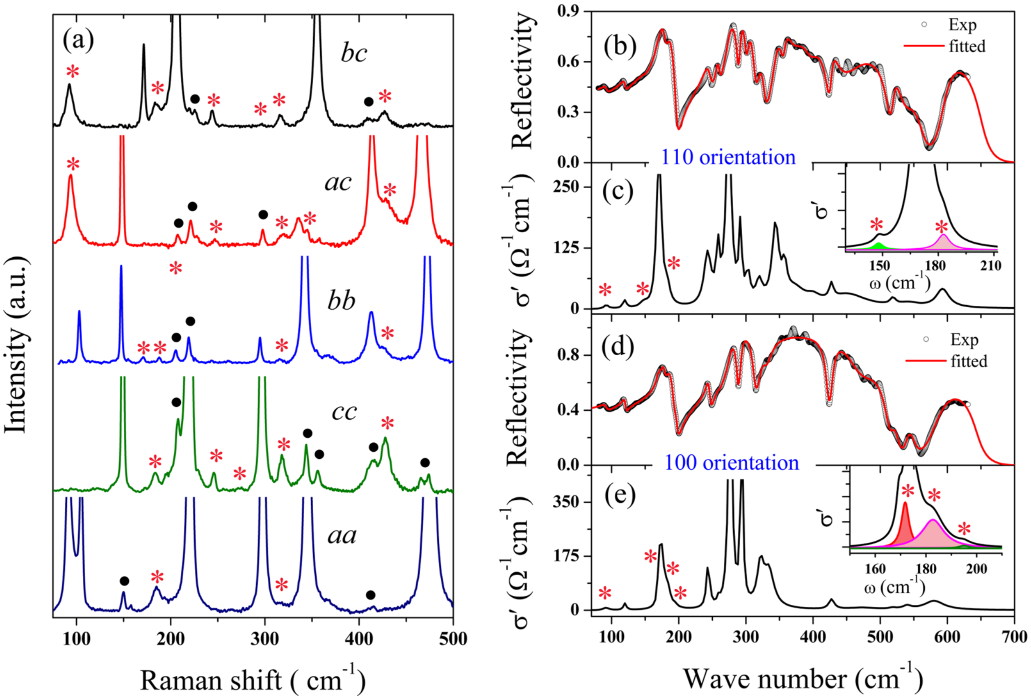

FIG. 5. (a) Raman spectra in various polarization configurations at 90 K. (b) and (d) give the IR spectra collected on (110)- and (100)-oriented single crystals at 90 K fitted with the Lorentz oscillator model (red line) and the obtained optical conductivity σ' (real) is shown in (c) and (e). The red stars indicate the new modes appearing below T_c and black dots mark the polarization leakage mode. The inset of (c) and (e) gives the magnified view of σ'. Color-shaded regions are the new IR modes obtained from the deconvolution of σ'.

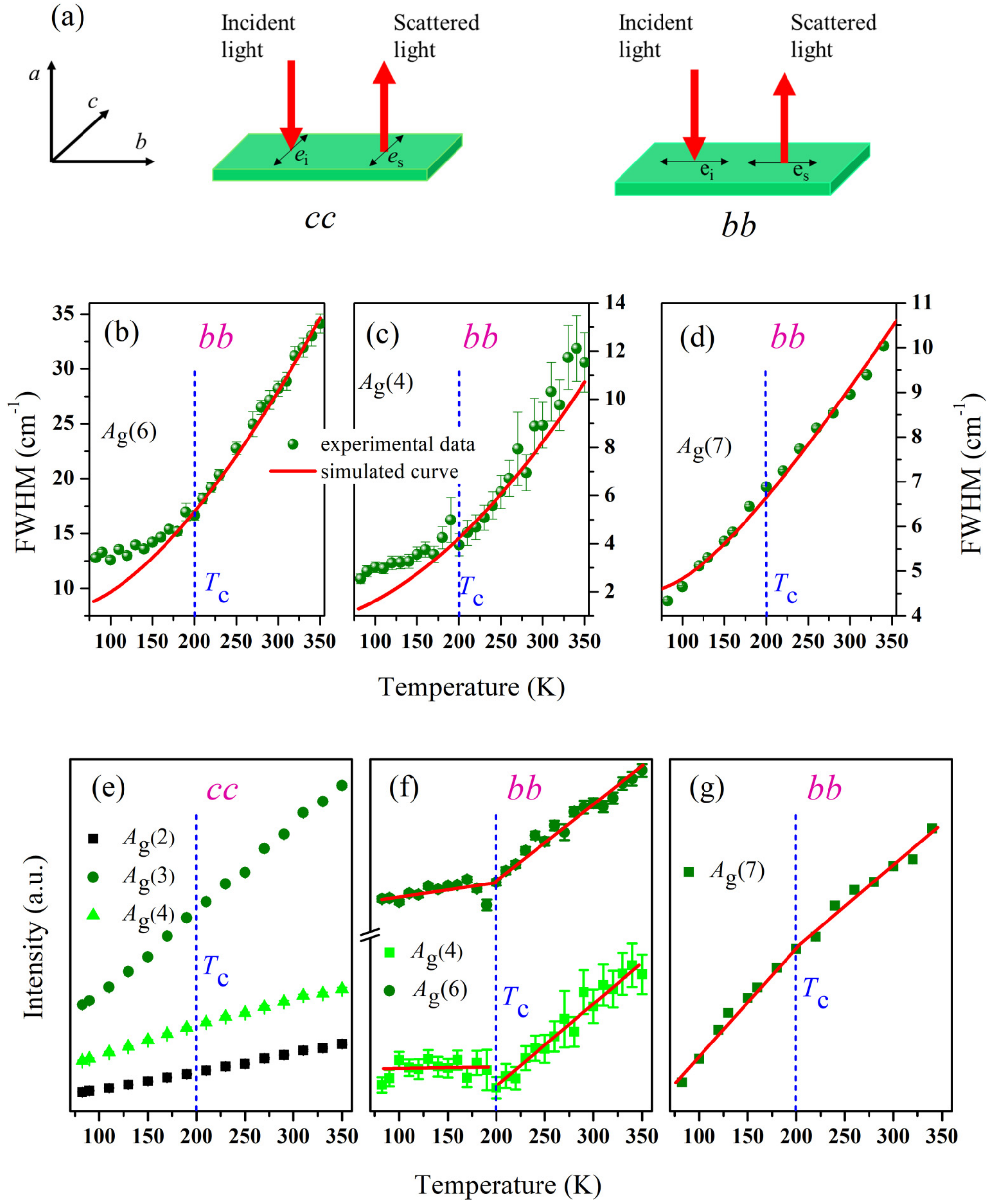

FIG. 7. *T*-dependent PRS study on an NGO (100) single crystal. (a) Schematic of the measurement geometries corresponding to the *bb* and *cc* polarization configurations along with the crystallographic axes. e_i and e_s denote the unit vectors representing electric field polarization of the incident and scattered light. *abc* represents the crystallographic axes. (b)–(g) show the *T* dependence of FWHM and intensity of some selected modes in two polarization configurations. The red solid curve in (b)–(d) is the anharmonic curve for four phonon decay processes, while the red line in (e)–(g) is the linear fit to the experimental data. The dashed vertical (blue) line marks T_c.

appears in the *aa* and *bb* polarization configurations while the $A_g(6)$ mode appears only in the *bb* polarization configuration. Therefore, the $A_g(7)$ mode will reflect changes in the *a* and/or *b* directions (i.e., *ab* plane) whereas the $A_g(6)$ mode reflects the change only along the *b* direction. The $A_g(7)$ mode represents in-phase octahedral stretching in the *ab* plane and in this mode, apical O atoms are stationary. Therefore, the intensity of this mode is expected to show a change only when the octahedral basal plane changes. On the other hand, $A_g(4)$ and $A_g(6)$ modes contain the apical O-atom vibrations. Therefore, the intensity of these modes will be influenced by the change in the octahedral basal plane and/or the change in apical O atoms. Thus, the monotonous *T* dependence of the $A_g(7)$ mode intensity and FWHM signifies a monotonous change in the *ab* plane whereas a drastic change in intensity and FWHM of the $A_g(4)$ and $A_g(6)$ modes across T_c signifies the displacement of apical O atoms across T_c. The *T* dependence of the intensity of the $A_g(4)$ and $A_g(6)$ modes change only in the *bb* polarization configuration, which confirms that the apical O atoms displace along the crystallographic *b* axis. The displacement of the apical O atoms along the *b* axis creates a further distortion in the oxygen octahedra across T_c. In the case of NGO this distortion is very small and therefore probably could not be detected by diffraction techniques. However, such a distortion was clearly seen by diffraction techniques in the isostructural compound $PbRuO_3$, in which this distortion is large [58]. In

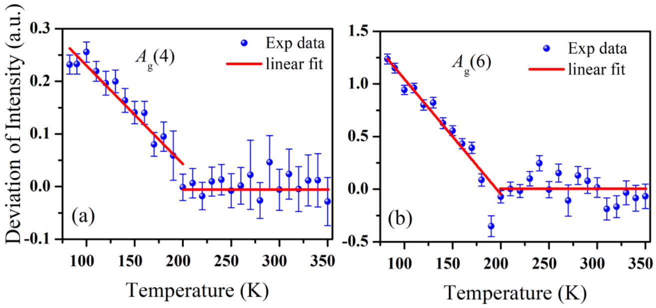

FIG. 8. Deviation of the Raman mode intensity as a function of temperature of the (a) $A_g(4)$ and (b) $A_g(6)$ modes in the *bb* polarization configuration. The red line represents the linear fitting of the experimental data.

Fig. 10 the schematic of the NGO structure in the *Pbnm* and $Pbn2_1$ space groups is presented. In the $Pbn2_1$ space group, the apical oxygen gets severely distorted while the basal plane oxygen remains unaffected and thus describes PRS results and a possible structure of NGO below T_c. It was suggested that such an octahedral distortion without much change in the basal plane is not possible in the *Pbnm* structure. Such an octahedral distortion was shown to be the cause for the structural phase transition from *Pbnm* to $Pbn2_1$ in $PbRuO_3$ and many other compounds [25,58,59]. The lattice parameters are very sensitive to octahedral distortions [60] and the displacement of the apical oxygen atoms along the *b* axis across T_c causes a change in the *b*-lattice parameter as reported previously through XRD measurements [10]. Cheng *et al.* [58] argued that in the $Pbn2_1$ structure, the enhanced octahedral distortion causes a significant increase in the cation orbital hybridization which displaces the cations from their centrosymmetric position and makes it noncentrosymmetric. This type of octahedral distortion was shown to be the root cause for the centrosymmetric to noncentrosymmetric phase transition in isostructural compounds such as $PbRuO_3$, $BiInO_3$, $CdTiO_3$ [25,58,61], and $NdGaO_3$ seems to follow this mechanism, although the displacement in this case is relatively small. Earlier, the anomaly in the various physical properties such as dielectric loss and magnetic susceptibility at T_c was explained considering subtle local structural modifications [14]. It was argued that the thermal factors (in XRD refinement) corresponding to the Nd and Ga atoms change at T_c, which produces the anomaly in the physical properties, however, the exact nature and cause for this change was not specified. Our experimental observations show ionic displacements at T_c producing a centrosymmetric to noncentrosymmetric phase transition which explains the anomalies in the physical properties across T_c. Actually, because of the strong correlation between thermal parameters and ionic displacements, the effect of ionic displacements can be compensated by the thermal parameters in refinements [62]. Therefore, the change in thermal factors shown by XRD refinement is basically arising from the ionic displacements at T_c.

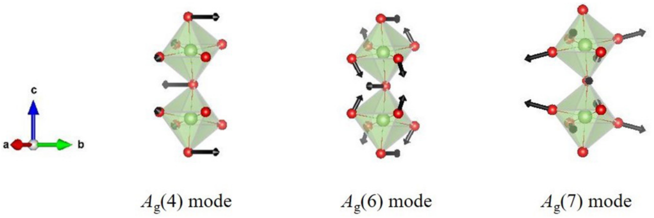

FIG. 9. Schematic lattice vibrations of some selected modes. The $A_g(4)$ mode represents the relative vibration of Nd and O atoms along the *b* axis. The $A_g(6)$ mode represents the out-of-phase octahedral bending vibration and the $A_g(7)$ mode represents the octahedral stretching vibration.

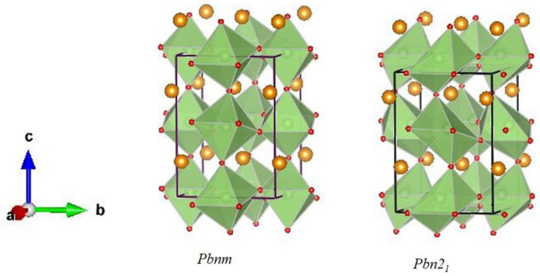

FIG. 10. Schematic representation of the octahedral distortion from the *Pbnm* to $Pbn2_1$ structures.

V. CONCLUSIONS

The crystal structure of the $NdGaO_3$ was studied from 350 down to 83 K using complimentary spectroscopic techniques, viz., Raman spectroscopy and IR spectroscopy along with theoretical calculations using DFT. The Raman and IR measurements showed a significant number of extra modes below 200 K and, importantly, some of the modes showed overlapping frequencies in the two measurements below 200 K. This gave direct evidence of the breaking of centrosymmetry below 200 K. The studied modes below and above 200 K matched well with the $Pbn2_1$ and *Pbnm* space groups, respectively, supporting the structural phase transition. The polarized Raman spectroscopy carried out under a unique protocol provided direct information about the root cause of the structural phase transition. Due to the increased distortion of the oxygen octahedra, the apical oxygen displaces along the *b* axis, causing the structural transition from a centrosymmetric to noncentrosymmetric space group.

ACKNOWLEDGMENT

Gaurav Sharma is acknowledged for discussions about the crystal structure analysis.

TABLE XIII. Relative change in slope in Raman intensity in comparison with a previous report.

Mode	α_1 (10^{-4})	$\alpha_{\text{deviation}}$ (10^{-4})	α_{norm}	From XRD (Ref. [10])
$A_g(4)$	19.3±0.9	18.7±1.8	0.9 ± 0.1	0.83
$A_g(6)$	137.7±7.4	109.3±7.38	0.79±0.06	

[1] J. M. Phillips, J. Appl. Phys. **79**, 1829 (1996); D. D. Castro, C. Cantoni, F. Ridolfi, C. Aruta, A. Tebano, N. Yang, and G. Balestrino, Phys. Rev. Lett. **115**, 147001 (2015).

[2] Y. Hu, M. Bator, M. Kenzelmann, T. Lippert, C. Niedermayer, C.W. Schneider, and A. Wokaun, Appl. Surf. Sci. **258**, 9323 (2012).

[3] H. Takahashi, J. Ohta, H. Fujioka, and M. Oshima, Thin Solid Films **407**, 114 (2002).

[4] L. C. Phillips, W. Yan, X. Moya, M. Ghidini, F. Maccherozzi, S. S. Dhesi, and N. D. Mathur, Phys. Rev. Appl. **4**, 064004 (2015).

[5] A. Senyshyn, L. Vasylechko, M. Knapp, U. Bismayer, M. Berkowski, and A. Matkovskii, J. Alloys Compd. **382**, 84 (2004).

[6] T. Ishichara, H. Matsuda, M. Azmi, B. Bustam, and Y. Takita, Solid State Ionics **86**, 197 (1996).

[7] S. Ghosh, S. Saha, Z. Liu, M. Motapothula, A. Patra, N. Yakovlev, Y. Cai, S. Prakash, X. H. Huang, C. B. Tay, C. X. Cong, T. Bhatt, S. B. Dolmanan, J. Chen, W. Lü, Z. Huang, S. Tripathy, S. J. Chua, T. Yu, M. Asta *et al.* Sci. Rep. **6**, 36352 (2016).

[8] S. Nakanishi and H. Itoh, Phys. Rev. B **59**, 5990 (1999).

[9] W. Marti, J. P. Rivera, F. Kubel, H. J. Scheel, and H. Schmid, Ferroelectrics **172**, 79 (1995).

[10] D. Savytskii, L. Vasylechko, A. Senyshyn, A. Matkovskii, C. Bahtz, M. L. Sanjuan, U. Bismayer, and M. Berkowski, Phys. Rev. B **68**, 024101 (2003).

[11] S. Geller, Acta Crystallogr. **10**, 243 (1957).

[12] W. Marti, P. Fischer, J. Schefer, and F. Kubel, Z. Kristallogr. **211**, 891 (1996).

[13] W. Marti, P. Fischer, F. Altorfer, H. J. Scheel, and M. Tadin, J. Phys.: Condens. Matter **6**, 127 (1994).

[14] L. Vasylechko, L. Akselrud, W. Morgenroth, U. Bismayer, A. Matkovskii, and D. Savytskii, J. Alloys Compd. **297**, 46 (2000).

[15] H. Brusset, M. H. Gillier-Pandraud, and J. B. Rdot, Bull. Soc. Chim. France **8**, 2886 (1967).

[16] E. Ito and Y. Matsui, Earth Planet. Sci. Lett. **38**, 443 (1978).

[17] A. Mock, R. Korlacki, S. Knight, M. Stokey, A. Fritz, V. Darakchieva, and M. Schubert, Phys. Rev. B **99**, 184302 (2019).

[18] J. Suda, T. Mori, H. Saito, O. Kamishima, T. Hattori, and T. Sato. Phys. Rev. B **66**, 174302 (2002).

[19] N. Rani, V. B. Gohel, H. C. Gupta, M. K. Singh, and L. M. Tiwari, J. Phys. Chem. Solids **62**1003 (2001).

[20] M. C. Saine, E. Husson, and H. Brusset, Spectrochim. Acta A **38**, 19 (1982).

[21] D. Nuzhnyy, J. Petzelt, S. Kamba, X. Marti, T. Cechal, C. M. Brooks, and D. G. Schlom, J. Phys.: Condens. Matter **23**, 045901 (2011).

[22] O. Kamishima, H. Koyama, R. Takahashi, Y. Abe, T. Sato, and T. Hattori, J. Phys.: Condens. Matter **14**, 3905 (2002).

[23] D. Savytskii, S. Ubizskii, A. Matkovskii, A. Suchocki, U. Bismayer, V. Pashkov, V. Borisov, A. Alexandrovskii, and A. Soldatov, Phase Transitions **70**, 57 (1998).

[24] E. Cohen, L. A. Risberg, W. A. Nornland, R. D. Burbank, R. C. Sherwood, and L. G. V. Uitert, Phys. Rev. **186**, 476 (1969).

[25] H. Moriwake, A. Kuwabara, C. A. J. Fisher, H. Taniguchi, M. Itoh, and I. Tanaka, Phys. Rev. B **84**, 104114 (2011).

[26] R. J. Birgeneau, J. K. Kjems, G. Shirane, and L. G. Van Uitert, Phys. Rev. B **10**, 2512 (1974).

[27] D. A. Long, *The Raman Effect: A Unified Treatment of the Theory of Raman Scattering by Molecules* (Wiley, Hoboken, NJ, 2002).

[28] S. Y. Chen, T. Goldstein, D. Venkataraman, A. Ramasubramaniam, and J. Yan, Nano Lett. **16**, 5852 (2016).

[29] K. Zhang, C. Bao, Q. Gu, X. Ren, H. Zhang, K. Deng, Y. Wu, Y. Li, J. Feng, and S. Zhou, Nat. Commun. **7**, 13552 (2016).

[30] T. C. Damen, S. P. S. Porto, and B. Tell, Phys. Rev. **142**, 570 (1966).

[31] A. B. Kuzmenko, Rev. Sci. Instrum. **76**, 083108 (2005).

[32] A. Togo and I. Tanaka, Scr. Mater. **108**, 1 (2015).

[33] G. Kresse and J. Furthmüller, Comput. Mater. Sci. **6**, 15 (1996).

[34] G. Kresse and D. Joubert, Phys. Rev. B **59**, 1758 (1999).

[35] J. P. Perdew, K. Burke, and M. Ernzerhof, Phys. Rev. Lett. **78**, 1396(E) (1997).

[36] J. P. Perdew, K. Burke, and M. Ernzerhof, Phys. Rev. Lett. **77**, 3865 (1996).

[37] H. J. Monkhorst and J. D. Pack, Phys. Rev. B **13**, 5188 (1976).

[38] F. Luis, M. D. Kuz'min, F. Bartolome, V. M. Orera, J. Bartolome, M. Artigas, and J. Rubin, Phys. Rev. B **58**798 (1998).

[39] See Supplemental Material at http://link.aps.org/supplemental/10.1103/PhysRevB.103.054106 for chatecterization of the single crystals, the Raman and IR fitted spectra, and the derivation of the relation between Raman tensor elements and strain components.

[40] Z. M. Zhang, B. I. Choi, M. I. Flik, and A. C. Anderson, J. Opt. Soc. Am. B **11**, 2252 (1994).

[41] S. Höfer, R. Uecker, A. Kwasniewski, J. Popp, and T. G. Mayerhöfer, Vib. Spectrosc. **78**, 17 (2015).

[42] R. Loudon, Adv. Phys. **13**, 423 (1964).

[43] J. Wu, N. Mao, L. Xie, H. Xu, and J. Zhang, Angew. Chem. **127**, 2396 (2015).

[44] K. Y. Choi, P. Lemmens, G. Guntherodt, M. Pattabiraman, G. Rangarajan, V. P. Gnezdilov, G. Balakrishnan, D. McK Paul, and M. R. Lees, J. Phys.: Condens. Matter **15**, 3333 (2003).

[45] M. Balkanski, R. F. Wallis, and E. Haro, Phys. Rev. B **28**, 1928 (1983).

[46] R. P. Bell and D. A. Long, Proc. R. Soc. London, Ser. A **203**, 364 (1950).

[47] D. W. Snoke and M. Cardona, Solid State Commun. **87**, 121 (1993).

[48] B. K. De, V. Dwij, R. Misawa, T. Kimura, and V. G. Sathe, J. Phys.: Condens. Matter **33**, 12LT01 (2021).

[49] A. Cui, Y. Ye, L. Zheng, K. Jiang, L. Zhu, L. Shang, Y. Li, Z. Hu, and J. Chu, Phys. Rev. B **100**, 024102 (2019).

[50] T. C. Wei, H. P. Wang, H. J. Liu, D. S. Tsai, J. J. Ke, C. L. Wu, Y. P. Yin, Q. Zhan, G. R. Lin, Y. H. Chu, and J. H. He, Nat. Commun. **8**, 15108 (2017).

[51] L. S. Schadler, S. C. Giannaris, and P. M. Ajayan, Appl. Phys. Lett. **73**, 3842 (1998).

[52] A. Antonakos, D. Palles, E. Liarokapis, M. Filippi, and W. Prellier, J. Appl. Phys. **104**, 063508 (2008).

[53] R. Korlacki, M. Stokey, A. Mock, S. Knight, A. Papamichail, V. Darakchieva, and M. Schubert, Phys. Rev. B **102**, 180101(R) (2020).

[54] J. Kreisel, A. M. Glazer, P. Bouvier, and G. Lucazeau, Phys. Rev. B **63**, 174106 (2001).

[55] A. Slodczyk, P. Daniel, and A. Kania, Phys. Rev. B **77**, 184114 (2008).

[56] G. Gibson, J. L. MacManus-Driscoll, and L. F. Cohen, IEEE Trans. Appl. Supercond. **7**, 2130 (1997).

[57] M. N. Iliev, M. V. Abrashev, H. G. Lee, V. N. Popov, Y. Y. Sun, C. Thomsen, R. L. Meng, and C. W. Chu, Phys. Rev. B **57**, 2872 (1998).

[58] J. G. Cheng, K. E. Kweon, J.-S. Zhou, J. A. Alonso, P. P. Kong, Y. Liu, C. Jin, J. Wu, J. F. Lin, S. A. Larregola, W. Yang, G. Shen, A. H. MacDonald, A. Manthiram, G. S. Hwang, and J. B. Goodenough, Proc. Natl. Acad. Sci. USA **110**, 20003 (2013).

[59] H. Taniguchi, Y. J. Shan, H. Mori, and M. Itoh, Phys. Rev. B **76**, 212103 (2007).

[60] M. W. Lufaso and P. M. Woodward, Acta Crystallogr., Sect. B **57**, 725 (2001).

[61] A. A. Belik, S. Y. Stefanovich, B. I. Lazoryak, and E. Muromachi, Chem. Mater. **18**, 1964 (2006).

[62] G. H. Kwei, A. C. Lawson, S. J. L. Billinge, and S. W. Cheong, J. Phys. Chem. **97**, 2368 (1993).